REPORT

QUANTUM CONTROL

Controlling quantum many-body dynamics in driven Rydberg atom arrays

D. Bluvstein[1], A. Omran[1,2], H. Levine[1], A. Keesling[1], G. Semeghini[1], S. Ebadi[1], T. T. Wang[1], A. A. Michailidis[3], N. Maskara[1], W. W. Ho[1,4], S. Choi[5], M. Serbyn[3], M. Greiner[1], V. Vuletić[6], M. D. Lukin[1]*

The control of nonequilibrium quantum dynamics in many-body systems is challenging because interactions typically lead to thermalization and a chaotic spreading throughout Hilbert space. We investigate nonequilibrium dynamics after rapid quenches in a many-body system composed of 3 to 200 strongly interacting qubits in one and two spatial dimensions. Using a programmable quantum simulator based on Rydberg atom arrays, we show that coherent revivals associated with so-called quantum many-body scars can be stabilized by periodic driving, which generates a robust subharmonic response akin to discrete time-crystalline order. We map Hilbert space dynamics, geometry dependence, phase diagrams, and system-size dependence of this emergent phenomenon, demonstrating new ways to steer complex dynamics in many-body systems and enabling potential applications in quantum information science.

Dynamics of complex, strongly interacting many-body systems have broad implications in quantum science and engineering, ranging from understanding fundamental phenomena (*1*, *2*) to realizing robust quantum information systems (*3*). Such dynamics typically lead to a rapid growth of quantum entanglement and a chaotic spreading of the wave function throughout an exponentially large Hilbert space, a phenomenon associated with quantum thermalization (*1*, *2*, *4*). Recent advances in the controlled manipulation of isolated, programmable many-body systems have enabled detailed studies of nonequilibrium states in strongly interacting quantum matter (*4*–*6*), in regimes inaccessible to numerical simulations on classical machines. Identifying nontrivial states for which dynamics can be stabilized or steered by external controls is a central question explored in these studies. For instance, it has been shown that strong disorder, leading to many-body localization (MBL), allows systems to suppress entanglement growth and retain memory of their initial state for long times (*7*, *8*). Another example involves quantum many-body scars, which manifest as periodic entanglement and disentanglement dynamics for special initial states that avoid rapid thermalization within an otherwise chaotic system (*9*–*11*). Further, periodic driving in strongly interacting systems can give rise to exotic nonequilibrium phases of matter, such as the discrete time crystal (DTC), which spontaneously breaks the discrete time-translation symmetry of the underlying drive (*12*, *13*). Here, we report the discovery of a new type of nonequilibrium dynamics associated with many-body scarring trajectories stabilized by periodic driving. The driven scars result in an emergent phenomenon akin to discrete time-crystalline order that can be harnessed to steer entanglement dynamics in complex many-body systems.

In our experiments, neutral ^{87}Rb atoms are trapped in optical tweezers and arranged into arbitrary two-dimensional patterns generated by a spatial light modulator (*14*, *15*). This programmable system allows us to explore quantum dynamics in systems ranging from chains and square lattices to exotic decorated lattices, with sizes up to 200 atoms. All atoms are initialized in an electronic ground state $|g\rangle$ and coupled to a Rydberg state $|r\rangle$ by a two-photon optical transition with an effective Rabi frequency $\Omega(t)$ and detuning $\Delta(t)$ (Fig. 1A). When excited into Rydberg states, atoms interact through a strong, repulsive van der Waals interaction $V \sim 1/d^6$, where d is the interatomic separation, resulting in the many-body Hamiltonian (*10*)

$$\frac{H}{\hbar} = \frac{\Omega(t)}{2}\sum_i \sigma_i^x - \Delta(t)\sum_i n_i + \sum_{i<j} V_{ij} n_i n_j \quad (1)$$

where $\hbar$ is the reduced Planck constant, $n_i = |r_i\rangle\langle r_i|$ is the projector onto the Rydberg state at site i, and $\sigma_i^x = |g_i\rangle\langle r_i| + |r_i\rangle\langle g_i|$ flips the atomic state. We choose lattice spacings where the nearest-neighbor (NN) interaction $V_0 > \Omega$ results in the Rydberg blockade (*14*, *16*, *17*), preventing adjacent atoms from simultaneously occupying $|r\rangle$. For large negative detunings, the many-body ground state is $|gggg\ldots\rangle$, and at large positive detunings on bipartite lattices, the ground state is antiferromagnetic, of the form $|rgrg\ldots\rangle$. Starting with all atoms in $|g\rangle$, adiabatically increasing Δ from large negative values to large positive values thus prepares antiferromagnetic initial states $|\mathrm{AF}\rangle$ (*10*, *18*–*21*); we choose array configurations (e.g., odd numbers of atoms) such that one of the two classical orderings, $|\mathrm{AF}_1\rangle$, is energetically preferred.

To explore quantum scarring in two-dimensional systems, we prepare $|\mathrm{AF}_1\rangle$ on an 85-atom honeycomb lattice and then suddenly quench at fixed Ω to a small positive detuning

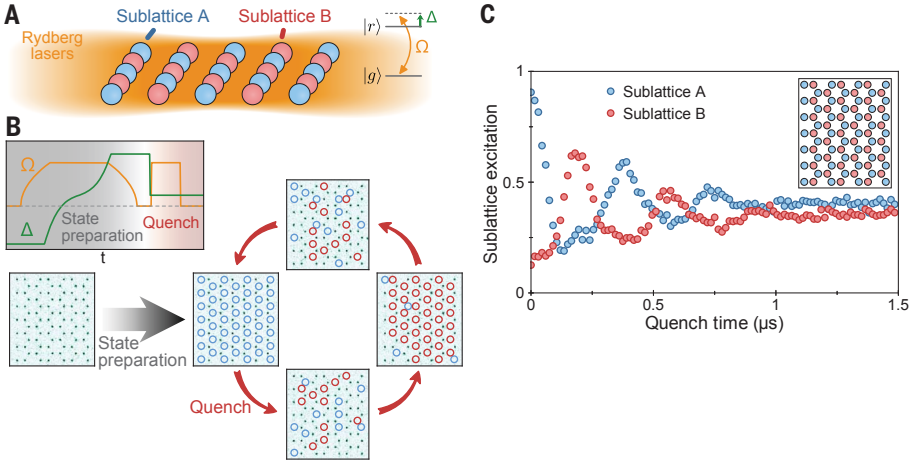

Fig. 1. Experimental investigations of quantum many-body scars. (**A**) Two-dimensional atom array subject to global Rydberg lasers with Rabi frequency Ω and detuning Δ. (**B**) A quasi-adiabatic ramp of Δ and Ω prepares an antiferromagnetic state $|\mathrm{AF}_1\rangle$ with sublattice A excited, and a detuning quench launches nonequilibrium dynamics. Atoms in $|g\rangle$ are imaged in optical tweezers by fluorescence, whereas atoms in $|r\rangle$ (empty circles) are expelled and detected as atom loss. (**C**) The Rydberg population on sublattices A and B undergoes periodic oscillations. The inset shows the geometry used here.

[1]Department of Physics, Harvard University, Cambridge, MA 02138, USA. [2]QuEra Computing Inc., Boston, MA 02135, USA. [3]IST Austria, Am Campus 1, 3400 Klosterneuburg, Austria. [4]Department of Physics, Stanford University, Stanford, CA 94305, USA. [5]Department of Physics, University of California Berkeley, Berkeley, CA 94720, USA. [6]Department of Physics and Research Laboratory of Electronics, Massachusetts Institute of Technology, Cambridge, MA 02139, USA.
*Corresponding author. Email: lukin@physics.harvard.edu

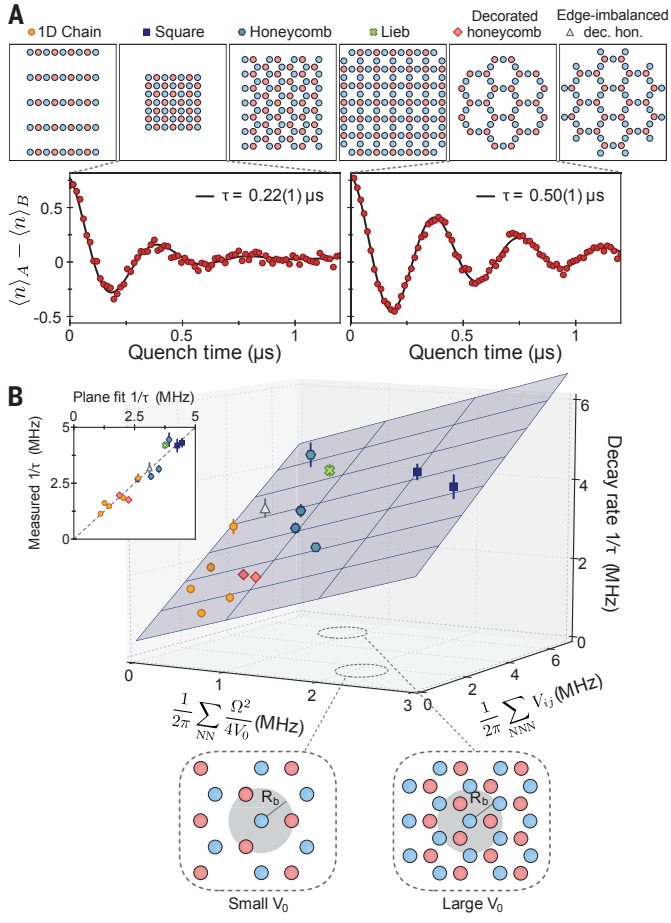

Fig. 2. Universal empirical description of scar lifetime. (**A**) Different geometries used in this study. The lifetime τ of the sublattice excitation difference depends strongly on the geometry. 1D stands for one-dimensional. (**B**) As a function of coupling to blockade-violating states ($\propto\Omega^2/V_0$) and NNN interactions, the scar decay rate $1/\tau$ displays a bilinear dependence. The inset shows a cross section of the plane. Schematics depict regimes where the two different decay processes dominate. Symbols are defined in (A). Error bars represent the standard error of the fit of τ.

(Fig. 1B). The system quickly evolves from $|\mathrm{AF}_1\rangle$ into a disordered state as expected from a thermalizing system, but then notably the opposite order $|\mathrm{AF}_2\rangle$ emerges at a later time (*11*). Through the same process, the system evolves back to $|\mathrm{AF}_1\rangle$, consistent with previous observations of quantum scars in one-dimensional chains (*10*, *11*). These scarring dynamics can be seen in the evolution of sublattice A and B populations as a function of quench duration (Fig. 1C), where disordered configurations arise when the sublattice populations are approximately equal. These observations are surprising in a strongly interacting system and indicate a special dynamical behavior as well as a form of ergodicity breaking (*11*, *22*). This scarring behavior is captured by the so-called "PXP" model of perfect NN blockade, in which V_0 is infinite and interactions beyond NN are zero: $H_{\mathrm{PXP}} = (\Omega/2)\sum_i P_{i-1}\sigma_i^x P_{i+1}$, where $P_i = |g_i\rangle\langle g_i|$ is the projector onto the ground state at site i. (*11*, *22*–*26*). In this model, the coherent oscillations of the sublattice population difference $\langle n\rangle_{\mathrm{A}} - \langle n\rangle_{\mathrm{B}}$ are understood as the oscillations of an emergent "large spin" (*27*).

We observe this oscillatory behavior in a wide variety of bipartite lattices (Fig. 2A). (We do not observe scarring on the nonbipartite lattices that we measure.) As an example, we plot the difference between the sublattice A and B populations $\langle n\rangle_{\mathrm{A}} - \langle n\rangle_{\mathrm{B}}$ for a 49-atom square and a 54-atom decorated honeycomb (*28*), with Rabi frequency $\Omega/2\pi = 4.2$ MHz and interaction strength $V_0/2\pi = 9.1$ MHz. We note a marked difference in the lifetime of periodic revivals for these two different lattices. Quantitatively, we find that dynamics of $\langle n\rangle_{\mathrm{A}} - \langle n\rangle_{\mathrm{B}}$ are well-described by a damped cosine, $y_0 + C\cos(\tilde{\Omega}t)\exp(-t/\tau)$, with oscillation frequency $\tilde{\Omega}$, decay time τ, offset y_0, and contrast C. Although $\tilde{\Omega} \approx 0.6\Omega$ on both the square and decorated honeycomb lattices (and on the other lattices we probe), the fitted τ for these two different configurations are 0.22(1) and 0.50(1) μs, respectively.

To understand this geometry dependence, we consider an empirical model for the decay rate of many-body scars [see (*29*)], parametrized as follows:

$$\frac{1}{\tau} = \alpha\left(\frac{1}{2\pi}\sum\nolimits_{\mathrm{NN}}\frac{\Omega^2}{4V_0}\right) + \beta\left(\frac{1}{2\pi}\sum\nolimits_{\mathrm{NNN}}V_{ij}\right) + \frac{1}{\tau_0} \qquad (2)$$

where the first two terms capture deviations of the Rydberg Hamiltonian from the idealized PXP model, owing to second-order virtual coupling to states violating blockade and next-nearest-neighbor (NNN) interactions, respectively (*29*); α, β, and τ_0 are phenomenological values. In Fig. 2B, we plot the measured $1/\tau$ as a function of the first and second terms in Eq. 2 for all geometries shown in Fig. 2A and varied interaction strengths V_0. We find that the decay rates fit well to a plane with slopes $\alpha = 0.72(12)$ and $\beta = 0.58(5)$ and offset $1/\tau_0 = 0.4(2)$MHz. Note that $1/\tau_0$, which includes decay contributions inherent to the idealized PXP model (*11*, *28*), is much smaller than $1/\tau$; i.e., the decay of scars is dominated by imperfect blockade and long-range interactions. The observation that long-range fields contribute to decay also motivates quenching to small positive $\Delta_{\mathrm{q}} = \Delta_{\mathrm{q,opt}} = 1/2\sum_{i,j>\mathrm{NN}}V_{ij}$, which cancels the static contribution from the long-range interactions (*29*) and is used throughout this work. These results also suggest an intrinsic limit to the scar lifetime, coming from the trade-off between imperfect blockade ($\propto 1/V_0$) and long-range interactions ($\propto V_0$). For example, we estimate a maximum lifetime $\tau_{\max} \approx 0.9$ μs for a chain and $\tau_{\max} \approx 0.4$ μs for a honeycomb lattice.

We next investigate the effect of parametric driving on many-body scars. To this end, we implement quenches to a time-dependent detuning $\Delta_{\mathrm{q}}(t) = \Delta_0 + \Delta_{\mathrm{m}}\cos(\omega_{\mathrm{m}}t)$, as illustrated in Fig. 3A, and explore a nonperturbative regime of $\Delta_{\mathrm{m}}, \Delta_0, \omega_{\mathrm{m}} \sim \Omega$. Notably, in Fig. 3B, we find that such a quench results in a fivefold increase of scar lifetime compared with the fixed-detuning case, for properly chosen drive parameters (modulation frequency $\omega_{\mathrm{m}} = 1.24\Omega$, offset $\Delta_0 = 0.85\Omega$, and amplitude $\Delta_{\mathrm{m}} = 0.98\Omega$ for this nine-atom chain). Further, we find that the drive changes the oscillation frequency $\tilde{\Omega}$ to $\omega_{\mathrm{m}}/2$, apparent in the synchronous revival of $\langle n\rangle_{\mathrm{A}} - \langle n\rangle_{\mathrm{B}}$ every two drive periods of $\Delta_{\mathrm{q}}(t)$.

Figure 3C shows the scar lifetime and oscillation frequency as a function of modulation frequency ω_{m}, for a nine-atom chain (with different V_0 than Fig. 3A), a 41-atom honeycomb, and a 66-atom edge-imbalanced decorated honeycomb [tabulation of system and drive parameters in (*29*)]. For all three lattices, a robust subharmonic locking of the scar frequency is observed at $\omega_{\mathrm{m}}/2$ over a wide range of ω_{m}, accompanied by a marked increase in the scar lifetime. The optimal driving frequency roughly corresponds to twice the natural scar oscillation frequency for the chain and honeycomb lattice (with an apparent ~10% shift toward lower ω_{m}), whereas the imbalanced lattice exhibits an unexpected double-peak structure (*29*). We note that sizable lifetime enhancements are found even when $\Delta_{\mathrm{m}}, \Delta_0 \gg \sum_{\mathrm{NNN}}V_{ij}$, and even in numerics for the idealized PXP model (*29*), indicating that the physical origin of the enhancement is not simply a mean-field-interaction cancellation akin to fixed $\Delta_{\mathrm{q,opt}}$.

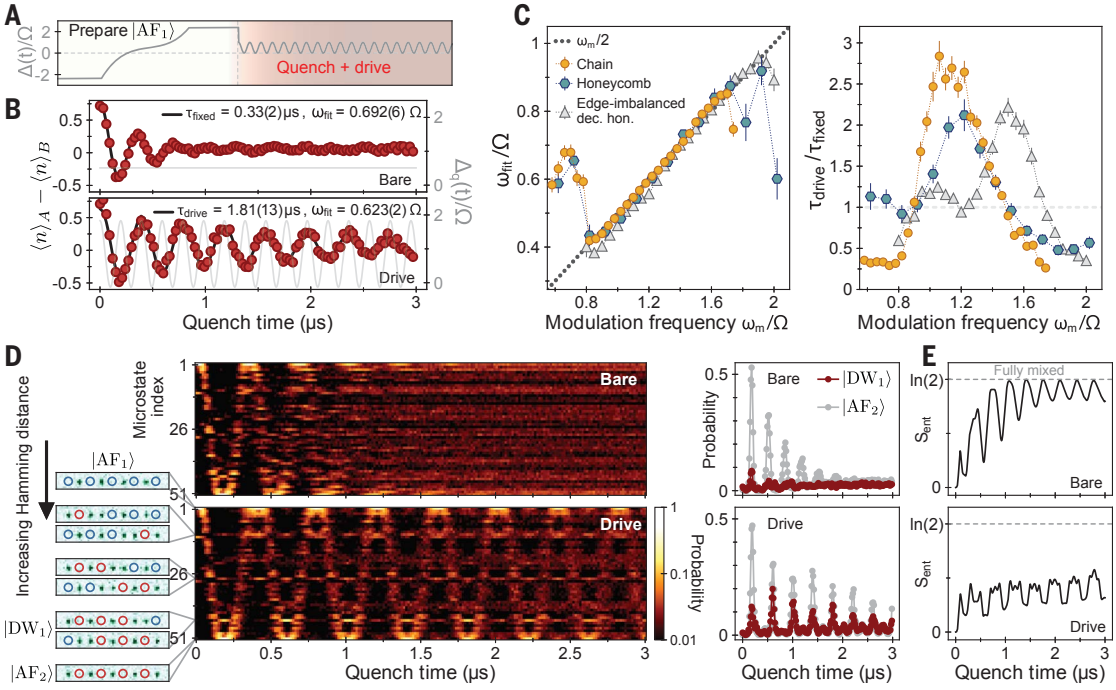

Fig. 3. Emergent subharmonic locking and stabilization. (**A**) Pulse sequence showing state preparation and quench with $\Delta_q(t)$. (**B**) Scar dynamics on a chain during quench to fixed optimal detuning (bare) with lifetime τ_{fixed}, and time-dependent detuning (drive) with modulation frequency $\omega_m = 1.24\Omega$ and lifetime τ_{drive}. The drive increases the scar lifetime and changes its frequency to $\omega_m/2$. (**C**) Scar response frequency and lifetime as a function of ω_m, showing a subharmonic locking and lifetime increase. (**D**) Dynamics of the entire Hilbert space measured with experimental snapshots (0.5 million total bit strings). The microstates of the constrained Hilbert space are ordered by $n_A - n_B$, or equivalently by Hamming distance (number of spin flips) from $|AF_1\rangle$ [see (*29*) for details]. Right subplots highlight $|AF_2\rangle$ and a state with a domain wall $|DW_1\rangle$. (**E**) Reduced density matrix of a single atom in a chain (numerics) shows that driving reduces the growth of entanglement entropy S_{ent}.

Figure 3D shows the experimentally observed distribution of microscopic many-body states across the entire Hilbert space of the nine-atom chain, as a function of quench time (see also movie S1). For the fixed detuning quench, oscillations between $|AF_1\rangle$ and $|AF_2\rangle$ product states are observed, before the quantum state spreads and thermalizes to a near-uniform distribution across the many-body states (*1*, *2*). Notably, parametric driving not only delays thermalization but also alters the actual trajectory being stabilized: The driven case also shows periodic, synchronous occupation of several other many-body states (emphasized in the right panels of Fig. 3D), seemingly dominated by those with near-maximal excitation number (indicated in the left panels). This suggests that rather than enhancing oscillations between the $|AF\rangle$ states, the parametric driving actually stabilizes the scar dynamics to oscillations between entangled superpositions composed of various product states. Figure 3E further illustrates the change in trajectory with numerical simulations of the local entanglement entropy, revealing that driving stabilizes the periodic entangling and disentangling of an atom with the rest of the system.

We observe this emergent subharmonic stabilization for a wide range of system and drive parameters. Figure 4, A and B, shows the time dynamics of $\langle n\rangle_A - \langle n\rangle_B$ and the normalized intensity of its associated Fourier transform $|S(\omega)|^2$ as a function of the drive frequency for a nine-atom chain. A response is observed at $\omega = \omega_m$ for $\omega_m < 0.8\Omega$, before suddenly transitioning into a subharmonic response $\omega = \omega_m/2$ for $\omega_m > 0.8\Omega$. For different drive parameters, a weak fourth subharmonic response at $\omega = \omega_m/4$ is also observed (*29*). To quantify the robustness of the observed response, we evaluate the subharmonic weight, $|S(\omega = \omega_m/2)|^2$, which encapsulates both the $\omega_m/2$ response and enhanced lifetime (*30*, *31*). Figure 4C shows the corresponding results for a nine-atom chain and a 41-atom honeycomb as a function of the modulation frequency ω_m and the lattice spacing a [in units of the blockade radius R_b defined by $V(R_b) = \Omega$]. A wide plateau in the subharmonic weight is clearly observed for both lattices, as a function of both modulation frequency and interaction strength (range 0.6 to $0.9a/R_b$ corresponds to $V_0/2\pi \approx 8$ to 80 MHz). To quantify the many-body nature of this stable region (*13*), we make use of the subharmonic rigidity, defined as the sum of the subharmonic weights measured at each modulation frequency: $\sum_{\omega_m} |S_{\omega_m}(\omega = \omega_m/2)|^2$ for $\omega_m = 0.75, 0.85, \ldots, 1.75\Omega$. The subharmonic rigidity quantifies robustness of the subharmonic response, where large values imply a large subharmonic response over a wide range of modulation frequencies. Figure 4D shows that subharmonic rigidity increases with system size until saturating at roughly 13 atoms for both a chain and a honeycomb lattice and appearing stable for the honeycomb lattice even to 200 atoms.

The emergent subharmonic response and its rigidity are strongly reminiscent of those associated with discrete time-crystalline order (*12*, *13*, *30*–*32*). Yet, there are clear distinctions. Specifically, this behavior is observed only for antiferromagnetic initial states, whereas other initial states such as $|ggg\ldots\rangle$ thermalize and do not show subharmonic responses (*29*). This sharp state dependence distinguishes these observations from conventional MBL or prethermal time crystals (*33*), where subharmonic responses are not tied to special initial states. Moreover, it is surprising that our drive, whose frequency is resonant with local energy scales, enhances quantum scarring and ergodicity breaking instead of rapidly injecting energy into the system, as would generally be expected in many-body systems (*34*).

To gain intuition into the origin of the observed subharmonic stabilization of many-body scars, we consider a toy, pulsed model with Floquet unitary $U_F(\theta, \tau) = e^{-i\theta\sum_i n_i} e^{-iH_{PXP}\tau}$, where rotation angle θ arises from an infinitesimal, strong detuning pulse [see the follow-up theoretical work (*35*)]. Owing to the particle-hole symmetry of the PXP Hamiltonian, for $\theta = \pi$, the time evolution $e^{-iH_{PXP}\tau}$ during one pulse is canceled by the time evolution $e^{iH_{PXP}\tau}$ in a subsequent pulse, generating an effective many-body echo and subharmonic response (*29*, *35*). Interestingly, for small deviations ε from perfect π rotations, giving rotation angles $\theta = \pi + \varepsilon$, revivals vanish for generic initial states but persist robustly for an initial $|AF\rangle$ state (*29*, *35*). This behavior can be

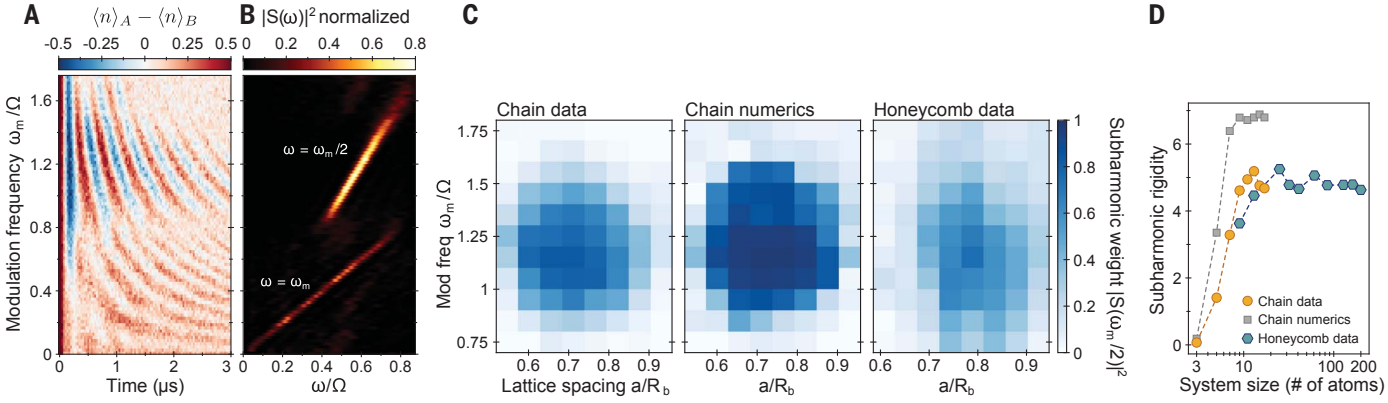

Fig. 4. Robustness of the subharmonic response. (**A**) Dynamics of sublattice population difference after quench, as a function of modulation frequency. (**B**) Fourier transform intensity $|S(\omega)|^2$ of data in (A), showing a harmonic locking for $\omega_m < 0.8\Omega$ and a subharmonic locking for $\omega_m > 0.8\Omega$. (**C**) Phase diagram of the subharmonic response $|S(\omega = \omega_m/2)|^2$ in chain data (left), chain numerics (middle) from perfectly initialized $|AF_1\rangle$ without experimental imperfections, and honeycomb data (right). (**D**) Increase of subharmonic rigidity (sum of subharmonic weights measured over a range of modulation frequencies) with increasing system size.

understood as follows: Owing to the scarring character of the antiferromagnetic initial states, the PXP evolution approximately realizes an effective π-pulse from $|AF_1\rangle$ to $|AF_2\rangle$ but results in ergodic spreading for other initial states. Accordingly, for $\theta = \pi + \varepsilon$, evolution still approximates an effective many-body echo for the scarred $|AF\rangle$ but does not reverse the chaotic evolution of generic initial states. Finally, the additional $\varepsilon\sum_i n_i$ serves as a "stabilizing Hamiltonian" by creating an effective gap between the $|AF\rangle$ states (which have maximal atomic excitations $n_{max} = \sum_i n_i$) from the rest of the spectrum. In practice, the $|AF\rangle$ states will be dressed by other states with near-maximal atomic excitations, consistent with the dynamics in Fig. 3D. Although the above arguments involve an idealized pulsed model, neglect large NNN interactions, and do not explicitly explain the observations in imbalanced lattices (Fig. 3C), this analysis already offers useful insight by connecting the observed subharmonic response to DTC physics (*35*) and warrants further study.

These considerations indicate that the observed subharmonic stabilization of many-body scars constitutes a new physical phenomenon that can be used for steering quantum dynamics in complex systems. Our observations challenge conventional understandings of quantum thermalization, warranting further investigation to understand the exact nature and conditions for this stabilization, its relationship to dynamical phases of matter such as the DTC, and the special role of the many-body scar states. Such studies could be extended to systems with more complex geometry, control, and topology, ranging from other initial states (*36*) and nonbipartite arrays (*14*, *21*) to the implementation of these techniques in other controllable many-body systems. These results open new possibilities for robust control of complex entangled states in many-body systems, with potential applications in areas such as quantum metrology and quantum information science (*3*).

REFERENCES AND NOTES

1. M. Srednicki, *Phys. Rev. E Stat. Phys. Plasmas Fluids Relat. Interdiscip. Topics* **50**, 888–901 (1994).
2. M. Rigol, V. Dunjko, M. Olshanii, *Nature* **452**, 854–858 (2008).
3. F. Arute *et al.*, *Nature* **574**, 505–510 (2019).
4. A. M. Kaufman *et al.*, *Science* **353**, 794–800 (2016).
5. M. Schreiber *et al.*, *Science* **349**, 842–845 (2015).
6. T. Langen *et al.*, *Science* **348**, 207–211 (2015).
7. D. A. Abanin, E. Altman, I. Bloch, M. Serbyn, *Rev. Mod. Phys.* **91**, 021001 (2019).
8. R. Nandkishore, D. A. Huse, *Annu. Rev. Condens. Matter Phys.* **6**, 15–38 (2015).
9. E. J. Heller, *Phys. Rev. Lett.* **53**, 1515–1518 (1984).
10. H. Bernien *et al.*, *Nature* **551**, 579–584 (2017).
11. C. J. Turner, A. A. Michailidis, D. A. Abanin, M. Serbyn, Z. Papić, *Nat. Phys.* **14**, 745–749 (2018).
12. V. Khemani, A. Lazarides, R. Moessner, S. L. Sondhi, *Phys. Rev. Lett.* **116**, 250401 (2016).
13. D. V. Else, B. Bauer, C. Nayak, *Phys. Rev. Lett.* **117**, 090402 (2016).
14. H. Labuhn *et al.*, *Nature* **534**, 667–670 (2016).
15. S. Ebadi *et al.*, arXiv:2012.12281 [quant-ph] (22 December 2020).
16. D. Jaksch *et al.*, *Phys. Rev. Lett.* **85**, 2208–2211 (2000).
17. E. Urban *et al.*, *Nat. Phys.* **5**, 110–114 (2009).
18. T. Pohl, E. Demler, M. D. Lukin, *Phys. Rev. Lett.* **104**, 043002 (2010).
19. P. Schauß *et al.*, *Science* **347**, 1455–1458 (2015).
20. E. Guardado-Sanchez *et al.*, *Phys. Rev. X* **8**, 021069 (2018).
21. V. Lienhard *et al.*, *Phys. Rev. X* **8**, 021070 (2018).
22. W. W. Ho, S. Choi, H. Pichler, M. D. Lukin, *Phys. Rev. Lett.* **122**, 040603 (2019).
23. C. Ates, J. P. Garrahan, I. Lesanovsky, *Phys. Rev. Lett.* **108**, 110603 (2012).
24. I. Lesanovsky, H. Katsura, *Phys. Rev. A* **86**, 041601 (2012).
25. C. J. Lin, O. I. Motrunich, *Phys. Rev. Lett.* **122**, 173401 (2019).
26. V. Khemani, C. R. Laumann, A. Chandran, *Phys. Rev. B* **99**, 161101 (2019).
27. S. Choi *et al.*, *Phys. Rev. Lett.* **122**, 220603 (2019).
28. A. A. Michailidis, C. J. Turner, Z. Papić, D. A. Abanin, M. Serbyn, *Phys. Rev. Res.* **2**, 022065 (2020).
29. Materials and methods are available as supplementary materials.
30. J. Zhang *et al.*, *Nature* **543**, 217–220 (2017).
31. S. Choi *et al.*, *Nature* **543**, 221–225 (2017).
32. N. Y. Yao, C. Nayak, L. Balents, M. P. Zaletel, *Nat. Phys.* **16**, 438–447 (2020).
33. D. V. Else, B. Bauer, C. Nayak, *Phys. Rev. X* **7**, 011026 (2017).
34. P. Ponte, A. Chandran, Z. Papić, D. A. Abanin, *Ann. Phys.* **353**, 196–204 (2015).
35. N. Maskara *et al.*, arxiv:2102.13160 [quant-ph] (25 February 2021).
36. B. Mukherjee, A. Sen, D. Sen, K. Sengupta, *Phys. Rev. B* **102**, 075123 (2020).

ACKNOWLEDGMENTS

We thank many members of the Harvard AMO community, particularly E. Urbach, S. Dakoulas, and J. Doyle for their efforts enabling safe and productive operation of our laboratories during 2020. We thank D. Abanin, I. Cong, F. Machado, H. Pichler, N. Yao, B. Ye, and H. Zhou for stimulating discussions. **Funding:** We acknowledge financial support from the Center for Ultracold Atoms, the National Science Foundation, the Vannevar Bush Faculty Fellowship, the U.S. Department of Energy (LBNL QSA Center and grant no. DE-SC0021013), the Office of Naval Research, the Army Research Office MURI, the DARPA DRINQS program (grant no. D18AC00033), and the DARPA ONISQ program (grant no. W911NF2010021). The authors acknowledge support from the NSF Graduate Research Fellowship Program (grant DGE1745303) and The Fannie and John Hertz Foundation (D.B.); a National Defense Science and Engineering Graduate (NDSEG) fellowship (H.L.); a fellowship from the Max Planck/Harvard Research Center for Quantum Optics (G.S.); Gordon College (T.T.W.); the European Research Council (ERC) under the European Union's Horizon 2020 research and innovation program (grant agreement no. 850899) (A.A.M. and M.S.); a Department of Energy Computational Science Graduate Fellowship under award number DE-SC0021110 (N.M.); the Moore Foundation's EPiQS Initiative grant no. GBMF4306, the NUS Development grant AY2019/2020, and the Stanford Institute of Theoretical Physics (W.W.H.); and the Miller Institute for Basic Research in Science (S.C.). **Author contributions:** D.B., A.O., H.L., A.K., G.S., S.E., and T.T.W. contributed to the building of the experimental setup, performed the measurements, and analyzed the data. A.A.M., N.M., W.W.H., S.C., and M.S. performed theoretical analysis. All work was supervised by M.G., V.V., and M.D.L. All authors discussed the results and contributed to the manuscript. **Competing interests:** M.G., V.V., and M.D.L. are co-founders and shareholders of QuEra Computing. A.O. is a shareholder of QuEra Computing. **Data and materials availability:** All data needed to evaluate the conclusions in the paper are present in the paper and the supplementary materials.

SUPPLEMENTARY MATERIALS

science.sciencemag.org/content/371/6536/1355/suppl/DC1
Materials and Methods
Figs. S1 to S13
Tables S1 and S2
References (*37*–*46*)
Movie S1

21 December 2020; accepted 12 February 2021
Published online 25 February 2021
10.1126/science.abg2530

Controlling quantum many-body dynamics in driven Rydberg atom arrays

D. Bluvstein, A. Omran, H. Levine, A. Keesling, G. Semeghini, S. Ebadi, T. T. Wang, A. A. Michailidis, N. Maskara, W. W. Ho, S. Choi, M. Serbyn, M. Greiner, V. Vuletic and M. D. Lukin

Science **371** (6536), 1355-1359.
DOI: 10.1126/science.abg2530originally published online February 25, 2021

Dynamic stabilization of an array

Large-scale systems comprising one-dimensional chains and two-dimensional arrays of excited atoms held in a programmable optical lattice are a powerful platform with which to simulate emergent phenomena. Bluvstein *et al.* built an array of up to 200 Rydberg atoms and subjected the system to periodic excitation. Under such driven excitation, they found that the array of atoms stabilized, freezing periodically into what looked like time crystals. Understanding and controlling the dynamic interactions in quantum many-body systems lies at the heart of contemporary condensed matter physics and the exotic phenomena that can occur.

Science, this issue p. 1355